

P- and *S*-wave delays caused by thermal plumes

Ross Maguire,¹ Jeroen Ritsema,¹ Peter E. van Keken,¹ Andreas Fichtner²
and Saskia Goes³

¹Department of Earth and Environmental Sciences, University of Michigan, Ann Arbor, MI 48109-1005, USA. E-mail: romaguir@umich.edu

²Institute of Geophysics, ETH Zürich, Zürich, Switzerland

³Department of Earth Science and Engineering, Imperial College London, London, SW7 2AZ, United Kingdom

Accepted 2016 May 16. Received 2016 March 1; in original form 2015 October 21

SUMMARY

Many studies have sought to seismically image plumes rising from the deep mantle in order to settle the debate about their presence and role in mantle dynamics, yet the predicted seismic signature of realistic plumes remains poorly understood. By combining numerical simulations of flow, mineral-physics constraints on the relationships between thermal anomalies and wave speeds, and spectral-element method based computations of seismograms, we estimate the delay times of teleseismic *S* and *P* waves caused by thermal plumes. Wave front healing is incomplete for seismic periods ranging from 10 s (relevant in traveltimes tomography) to 40 s (relevant in waveform tomography). We estimate *P*-wave delays to be immeasurably small (<0.3 s). *S*-wave delays are larger than 0.4 s even for *S* waves crossing the conduits of the thinnest thermal plumes in our geodynamic models. At longer periods (>20 s), measurements of instantaneous phase misfit may be more useful in resolving narrow plume conduits. To detect *S*-wave delays of 0.4–0.8 s and the diagnostic frequency dependence imparted by plumes, it is key to minimize the influence of the heterogeneous crust and upper mantle. We argue that seismic imaging of plumes will advance significantly if data from wide-aperture ocean-bottom networks were available since, compared to continents, the oceanic crust and upper mantle are relatively simple.

Key words: Body waves; Computational seismology; Wave scattering and diffraction; Wave propagation; Oceanic hotspots and intraplate volcanism; Dynamics: convection currents, and mantle plumes.

1 INTRODUCTION

Hotspots (Wilson 1963) and mantle plumes (Morgan 1971) have been important concepts in global geophysical and geochemical research (Ballmer *et al.* 2015) for more than half a century. In the classical view, plumes begin as thermal instabilities at the core–mantle boundary (CMB) and rise rapidly through the mantle. The voluminous plume head erupts as flood basalts to form large igneous provinces. The narrow plume tail is a persistent source of volcanism with a relatively fixed mantle position.

While plumes explain broad topographic swells, geoid highs and the distinct geochemistry of basalts at hotspots, the plume hypothesis has not been universally accepted. A number of hotspots may not require a deep mantle origin (e.g. King & Ritsema 2000) and plumes in a heterogeneous mantle with chemical and phase changes are predicted to be more complex than plumes in the classical models (e.g. Samuel & Farnetani 2003; Lin & van Keken 2006; Ballmer *et al.* 2013). Seismic images (e.g. Bijwaard & Spakman 1999; Allen 2002; Montelli *et al.* 2004; Wolfe *et al.* 2009; Styles *et al.* 2011; French & Romanowicz 2015) and statistical analyses (Boschi *et al.* 2007, 2008) suggest that several low-velocity anomalies are contin-

uous from the top to the bottom of the mantle. In addition, mantle transition zone thinning has been observed beneath a number of hotspots (e.g. Shen *et al.* 1998; Schmandt *et al.* 2012), potentially indicating a thermal anomaly extending to the lower mantle. Yet, it remains controversial to associate the complex seismic observations and models uniquely to thermal plumes.

Several factors complicate the resolution of the seismic structure of the mantle beneath hotspots. First, most regional seismic networks, and especially those covering oceanic hotspots (i.e. Hawaii and Iceland), have limited aperture. The sparse wave-path coverage in the lower mantle leads to overwhelming seismic modeling artefacts. Second, the deceleration of waves traversing a plume tail may not be recorded at seismic stations on the surface due to the destructive interference of direct and diffracted waves (i.e. wave front healing) (Nolet & Dahlen 2000; Malcolm & Trampert 2011). These diffractions, recorded in the coda of *P* and *S* waves (Rickers *et al.* 2012), are weaker than the coda signals produced by scattering in the crust.

To make meaningful interpretations of seismic data and models, it is important to understand the expected imprint of plumes in waveforms. In this paper, we estimate the delay times of *S* and

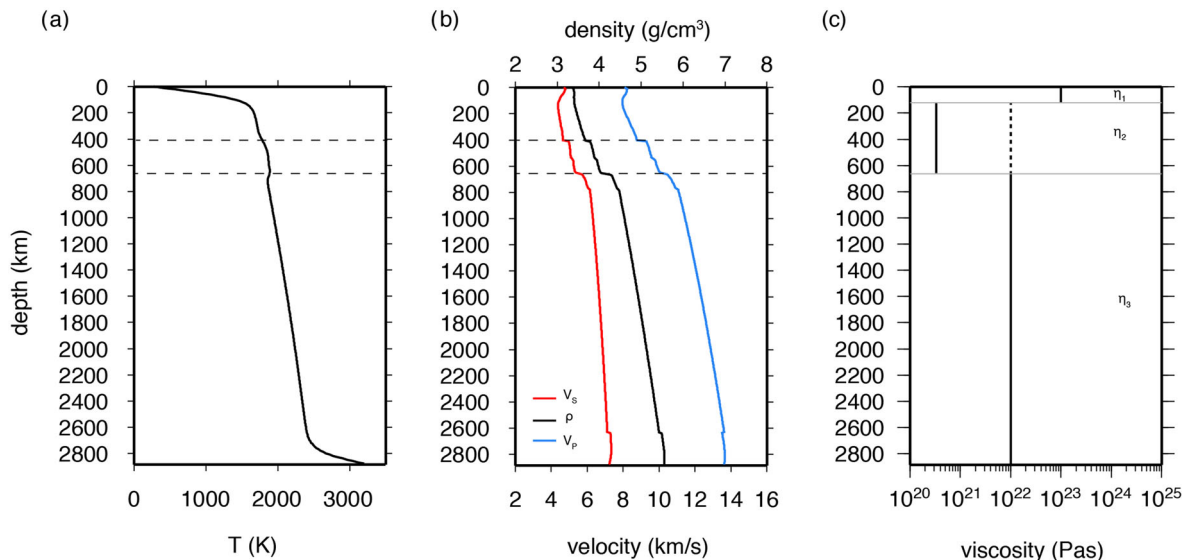


Figure 1. Reference profiles for (a) temperature and (b) V_S (red line), V_P (blue line) and density (black line). Reference values are calculated along the reference geotherm of the dynamic plume models. Note the anomalous changes in temperature, V_S , V_P , and density near the 410- and 660-km phase transitions (dashed lines) due to latent heat effects. (c) Prefactors of three-layer viscosity profile $\eta(z)$: $\eta_3 = 10^{22}$ Pa s in the lower mantle, $\eta_1 = 100 \eta_3$ in the lithosphere, $\eta_2 = \eta_3$ or $\eta_2 = \eta_3/30$ in the upper mantle.

P waves, which are principal observations used in traveltime tomography. We develop seismic models of plumes by combining numerical simulations of flow and mineral-physics constraints on the relationships between thermal anomalies and wave speeds. We use 3-D spectral-element method computations to synthesize teleseismic S - and P -wave propagation through plumes at frequencies up to 0.1 Hz, which are relevant in body-wave analyses. This work builds on analyses of uniform cylindrical anomalies (Rickers *et al.* 2012) and on analyses of 2.5-D axisymmetric synthetics (Hwang *et al.* 2011).

Our seismic models of axisymmetric plumes are based on plume ascent in a compressible mantle with an isochemical pyrolitic composition and with phase changes. We vary the strength and width of plumes by varying the dynamic parameters. The plume buoyancy fluxes are about $2 \times 10^3 \text{ kg s}^{-1}$ in the lower mantle, which are within the range of the fluxes inferred from hotspot swell topography (Sleep 1990). It is likely that plumes in the Earth deviate substantially from our idealized numerical models due to, for example, entrainment of compositionally distinct material (e.g. Lin & van Keken 2006; Samuel & Bercovici 2006; Kumagai *et al.* 2008) and the shearing by the overriding plate (Ballmer *et al.* 2015). However, we focus primarily on the structure of the narrow, vertical plume conduit, whose seismic resolvability in the lower mantle is uncertain. Any deviation from an idealized vertical conduit due to large-scale flow is unlikely to significantly alter the width of the plume tail, or the amplitude of the seismic anomaly.

2 NUMERICAL SIMULATIONS

2.1 Thermal plumes in a compressible mantle

We simulate plumes closely following Bossmann & van Keken (2013), in which we solve the equations governing conservation of mass, momentum and energy as defined by the anelastic liquid approximation (Jarvis & McKenzie 1980). The equations are

discretized via the finite-element method and solved in an axisymmetric spherical shell. We use a staggered grid refinement scheme to optimize the computations. The smallest grid spacing of 2.85 km is necessary to resolve the high-temperature gradients in the plume head. The bottom boundary is a free-slip surface with a fixed temperature of 3270 K. The side wall is insulating and the top boundary is fixed at 273.15 K. Rigid boundaries at the top and side of the domain limit large-scale horizontal flow and emphasize plume development.

The initial adiabatic temperature profile (Fig. 1) is determined using the Adams–Williamson equation of state. Estimates of the temperature increase across the superadiabatic thermal boundary layer above the CMB range from 500 to 1800 K (Lay *et al.* 2008). We vary the temperature contrast, ΔT_{CMB} , across the basal thermal boundary layer between 550 and 750 K. The depth-dependent thermal expansivity, α , decreases by a factor of three from the Earth’s surface to the CMB. A surface value of thermal expansivity, $\alpha_0 = 3 \times 10^{-5} \text{ K}^{-1}$ and specific heat, $c_p = 1250 \text{ J kg}^{-1} \text{ K}^{-1}$ yield a dissipation number $\text{Di} = 0.679$ for all plume models.

Viscosity, η , varies as a function of temperature T and depth z

$$\eta(T, z) = \eta(z) e^{-b(T - T^*)}. \quad (1)$$

A linearization of the Arrhenius viscosity law for diffusion creep with $E = 300 \text{ kJ mol}^{-1}$ (e.g. Karato & Wu 1993) yields a viscosity reduction between one and three orders of magnitude over the range of plume excess temperatures we consider (i.e. $b = \ln(10)$ to $\ln(1000)$). The depth-dependent viscosity prefactor $\eta(z)$ is given by three layers (Fig. 1c). The viscosity in the lower mantle, η_3 , is 10^{22} Pa s. A stiff upper layer of $\eta_1 = 100 \eta_{\text{LM}}$ simulates a 120-km-thick lithosphere. The viscosity η_2 in the upper mantle is either η_3 or $\eta_3/30$.

Plumes are initiated by applying a cosine perturbation to the basal thermal boundary layer. The peak perturbation at the symmetry axis is equal to half of the temperature difference between the surface and the CMB. We vary the structure of plumes by modifying the radial viscosity profile, the temperature dependence of rheology, the temperature contrast across the basal thermal boundary layer

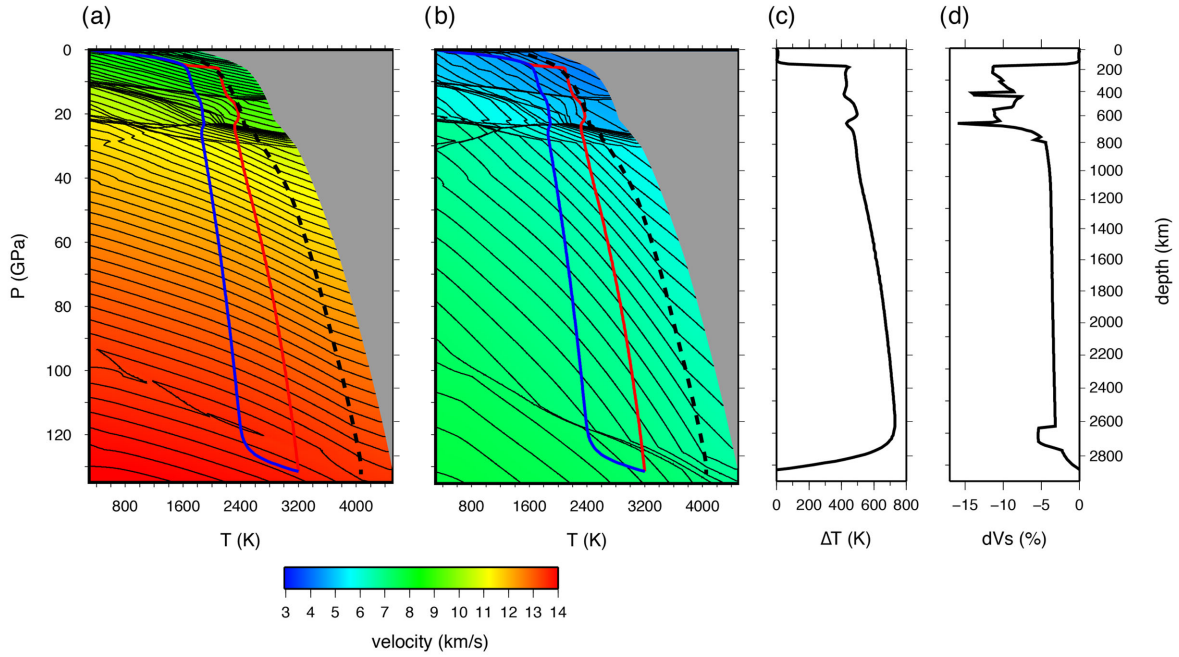


Figure 2. (a) V_P and (b) V_S as a function of pressure and temperature. The blue line is the geotherm for the reference structure. The red line is the geotherm along the plume axis of model R1b. The dry solidus of pyrolite is shown as a bold dashed line. Seismic velocity contours are shown every 0.1 km s^{-1} . (c) Plume excess temperature, ΔT and (d) shear velocity reduction along the axis of plume R1b. Peaks near 410 and 660 km depth are due to phase transitions.

and phase changes in the mantle transition zone. Plumes are broad in a mantle with relatively high viscosity and localized when rheology is strongly temperature dependent. The endothermic phase transition at the base of the mantle transition zone can inhibit plume ascent.

Phase functions describe the relative fraction of each mineral phase as a function of excess pressure at the 410- and 660-km phase transitions. For models considering phase changes, we assume that the Clapeyron slopes of the olivine-wadsleyite phase change (Γ_{410}) and the ringwoodite-perovskite phase change (Γ_{660}) are $+3.8$ and -2.5 MPa K^{-1} , respectively. The effects of latent heat on temperature are included in the reference temperature profile.

Plume excess temperature in the upper mantle inferred from OIB major-element geochemistry is expected to be in the range of 100–300 K (e.g. Courtier *et al.* 2007). Here, plume models slightly exceed this range (~ 350 –500 K) for the upper mantle. This is potentially due to a lack of lateral motion imposed by the axisymmetric constraint. It may also be an indication that plumes in the Earth carry a fraction of the heat from the CMB to the surface, potentially due to chemical stratification of a dense layer above the core (e.g. Farnetani 1997). Stagnation just below the transition zone may also promote cooling (e.g. Ballmer *et al.* 2015). Our models neglect latent heat loss due to melting, but this is likely a second-order effect.

We calculate the buoyancy flux B by integrating the product of mass flux and thermal expansion due to the plume excess temperature over a spherical surface S with a radius of 10° , centred on the plume axis.

$$B = \int \rho \alpha w (T - T_A) dS, \quad (2)$$

where ρ is density, α is thermal expansivity, w is the upward velocity and T_A is the adiabatic reference temperature. Further details are provided in Bossmann & van Keken (2013).

2.2 Seismic velocity conversion

The P -wave (V_P) and S -wave (V_S) velocity structure of the plume is determined using thermodynamic first principles. We assume a pyrolite mantle composition (Workman & Hart 2005) and the elastic parameter database described in Stixrude & Lithgow-Bertelloni (2011) for the six oxides SiO_2 , MgO , FeO , CaO , Al_2O_3 and Na_2O . Mineral parameters in the database are calculated for a third-order, finite-strain equation of state with Mie–Grüneisen temperature correction. We use the PerPleX software (Connolly 2005) to compute an equilibrium mineral assemblage at each point in P and T . V_P and V_S of a bulk mineral assemblage is determined by Voigt–Reuss–Hill averaging of the velocities of each constituent phase (Figs 2a and b). The effects of anelasticity on shear wave velocity are incorporated using a model for the S -wave quality factor Q_S that varies with temperature T and depth z as $Q_S(z, T) = Q_o \omega^a \exp(\frac{a\xi T_m}{T})$, where ω is frequency, a is exponential frequency dependence, ξ is a depth scaling factor and T_m is the dry solidus melting temperature. Our anelasticity model, Q7g uses values of $Q_o = 0.1, 0.5, 1.5$ for the upper mantle, transition zone and lower mantle, respectively. ξ in these intervals is 38, 30 and 26. The frequency ω is assumed to be $1/20 \text{ Hz}$ and a is assumed to be 0.15. We use the dry solidus calculated in Herzberg *et al.* (2000) for the upper mantle and Zerr *et al.* (1998) for the lower mantle. The calculation of V_P and V_S is not well defined where partial melt is present, which may occur in the shallow plume head. We estimate reductions in seismic velocity at temperatures above the dry solidus by linear extrapolation using the local temperature derivatives at the solidus.

A maximum plume temperature anomaly of 750 K in the lower mantle corresponds to shear velocity reductions of up to 4 per cent. Although plume excess temperature is smaller in the upper mantle, the shear velocity reduction is, on average, about 10 per cent along the plume axis. Maximum shear velocity reductions of 15 per cent near 410 and 660 km depth are due to perturbations of the phase-transition depth.

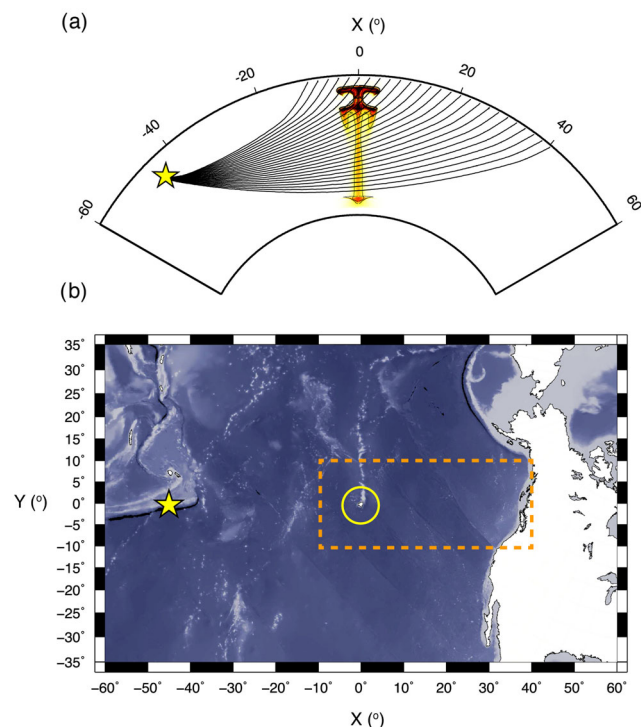


Figure 3. (a) Vertical cross-section of the geometry of the seismic model. Plume R1b is at $X = 0$, the earthquake at $X = -45^\circ$ and a depth of 400 km. The black lines are ray paths to illustrate the P and S propagation through the plume. (b) Map view representing the geometry of the model domain. The domain spans 120 degrees in X and 70° in Y . The earthquake (yellow star), plume (yellow circle) and a grid of seismic stations (dashed line) represents a hypothetical seismic deployment designed to image the mantle beneath Hawaii using recordings of earthquakes in the Fiji–Tonga region at stations in the NE Pacific.

2.3 3-D waveform computations

We compute the full 3-D wavefield using the spectral element solver SES3D (Gokhberg & Fichtner 2015), which solves the integral form of the elastic wave equation in a heterogeneous media. We simulate signals with periods between 10 and 200 s using a bandpass filtered Heaviside source time function. The simulation of $T > 10$ s waveforms for 30-min long seismograms is computed in approximately 30 min real time on 864 parallel compute nodes, each equipped with a GPU accelerator.

The computational domain is a spherical shell that spans 120° in longitude, 70° in latitude and 2500 km in depth. The domain consists of 4.68×10^7 elements and 5.85×10^9 gridpoints to ensure that at least two elements sample the shortest wavelengths (≈ 40 km).

We place the earthquake source at 400 km depth in order to avoid interference of direct waves and depth phases. The plume axis is 45° from the source (Fig. 3) so direct S and P waves simulated for teleseismic distances (30° – 80°) do not interact with the core. We calculate seismograms for the reference background model and each plume model at a grid of stations behind the plume axis (Fig. 3b). This geometry represents a hypothetical seismic experiment in the NE Pacific designed to image the mantle structure beneath Hawaii using recordings of earthquakes in the Tonga–Fiji region.

Synthetic seismograms for plume model R1b (Fig. 4) show delays and waveform complexity as a function of distance, which are typical for all plume models. Waveform complexity near $X = 4^\circ$ is

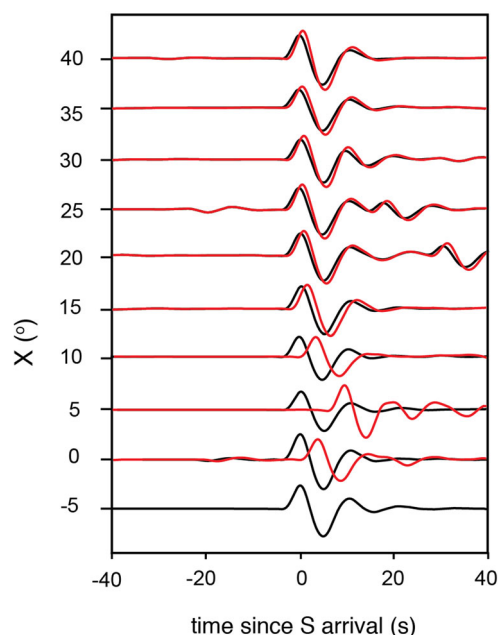


Figure 4. S waveforms for the background model (black) and plume model R2 (red) as a function of distance X from the plume axis. The waveforms have a minimum period $T = 10$ s. They have been aligned on the theoretical arrival time of the S wave for the background model.

due to multipathing as S interacts with the strong wave speed gradients at the margins of the plume head. For $X > 8^\circ$, when S crosses the plume axis in the lower mantle, waveforms for plume R1b and the background model are nearly identical except for a time offset (i.e. the traveltime delay). For increasing X , the traveltime delay diminishes from about 3 s at $X = 10^\circ$ to about 0.5 s at $X = 40^\circ$. Wave diffraction around the plume conduits is not clearly visible in the S coda at 10 s period.

3 DYNAMIC PLUME MODELS

We simulate four seismic structures for three plumes with different morphologies by modifying the thermal Rayleigh number Ra , η , ΔT_{CMB} and by incorporating phase changes (Fig. 5 and Table 1). We choose a limited set of plumes because of the computationally expensive waveform simulations. However, they represent the range of widths and strengths of plume conduits in the lower mantle and the range of expected P -wave and S -wave delays.

Plume models R1a and R1b represent two stages of evolution of the same plume. This plume ascends in a mantle with moderately temperature-dependent rheology ($b = \ln(10^2)$), a thermal Rayleigh number of 2×10^6 and with phase transitions. $\Delta T_{\text{CMB}} = 750$ K, which renders an excess temperature in the upper mantle of ~ 450 K. The viscosity in the upper mantle is $30\times$ smaller than the viscosity in the lower mantle, that is, $\eta_2 = \eta_3/30$. At 45 Myr (model R1a), the broad plume head is still in the lower mantle. At 55 Myr (model R1b), the plume head has crossed the upper-mantle transition zone and begins to spread beneath the lithosphere, and its conduit has narrowed due to the reduction in viscosity. Reductions of V_S are as large as 15 per cent in the plume head. The tail has a diameter of 200 km and V_S has been reduced by up to 4 per cent. We define plume tail width to be the point at which plume excess temperature

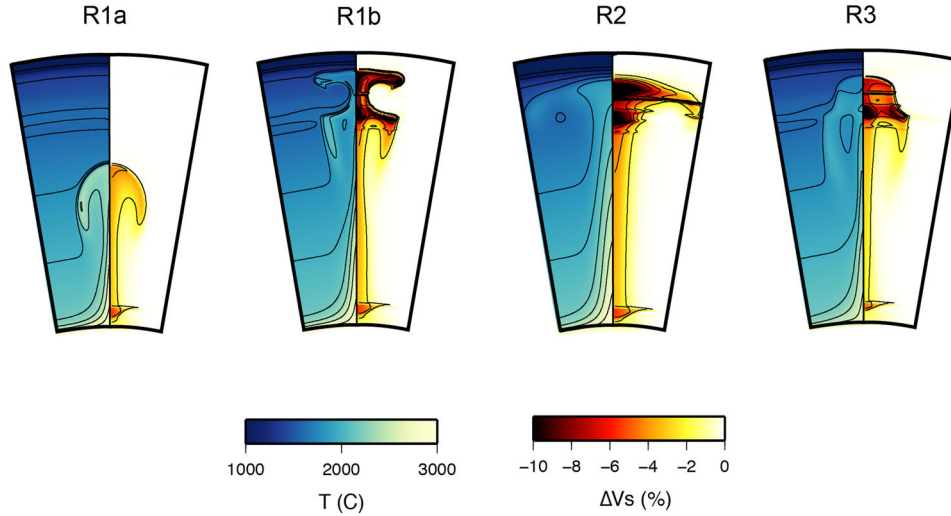


Figure 5. The temperature field (left half) and S -wave velocity perturbations ΔV_S (right half) of plume models R1a, R1b, R1c, R2 and R3. ΔV_S is relative to the reference shear velocity profile in shown in Fig. 1. Temperature and ΔV_S contours are shown every 200 K and every 2 per cent, respectively. The cross-sections are 20° wide and extend from the surface to the core–mantle boundary.

Table 1. Physical parameters used in plume simulations.

	Ra	Time (Myr)	ΔT_{CMB} (K)	b	B (Mg s^{-1})	Phase changes
R1a	2×10^6	45	750	$\ln(10^2)$	2.00	Yes
R1b	2×10^6	55	750	$\ln(10^2)$	2.91	Yes
R2	1×10^6	201	750	$\ln(10)$	1.94	No
R3	8×10^5	106	550	$\ln(10^3)$	1.87	Yes

diminishes to half of the maximum value at a given depth, as in Goes *et al.* (2004).

Plume R2 ascends in a mantle with weakly temperature-dependent viscosity ($b = \ln(10)$), a thermal Rayleigh number $Ra = 10^6$ and $\Delta T_{\text{CMB}} = 750$ K. We omit the effect of phase changes and the viscosity $\eta_2 = \eta_3 = 10^{22}$ Pa s in both the upper and lower mantle, which leads to a more simple lower-mantle structure in contrast to R1b. Plume R2 is sluggish because of the weak temperature dependence of viscosity and the low Ra . Its rise time is ≈ 200 Myr as opposed to ≈ 50 Myr for R1b. The plume tail has a diameter of about 400 km in the lower mantle. Without the viscosity reduction in the upper mantle, the plume conduit remains broad after crossing the 660-km phase transition. Although the viscosity structure and Rayleigh number differ significantly, the temperature and V_S along the plume axis in models R1b and R2 are similar because the excess temperature in the upper mantle is primarily controlled by the dissipation number Di and ΔT_{CMB} (Albers & Christensen 1996).

The plume in model R3 has developed in a relatively weak thermal boundary layer ($\Delta T_{\text{CMB}} = 550$ K), and it has a relatively small excess temperature (≈ 350 K) at the base of the lithosphere. The mantle has a rheology with strong temperature dependence ($b = \ln(10^3)$). As in R1a and R1b, we incorporate a viscosity reduction by a factor of 30 in the upper mantle and the effects of phase changes in the transition zone. The thermal Rayleigh number $Ra = 8 \times 10^5$. The plume tail is narrow (150 km in diameter) and V_S reductions are smaller than in R1a, R1b and R2. The thin and weak tail of R3 may be the most challenging to image seismically. As plumes R1b and R3 evolve further in time the tails broaden slightly, as they no longer feel the pull of the buoyant plume head.

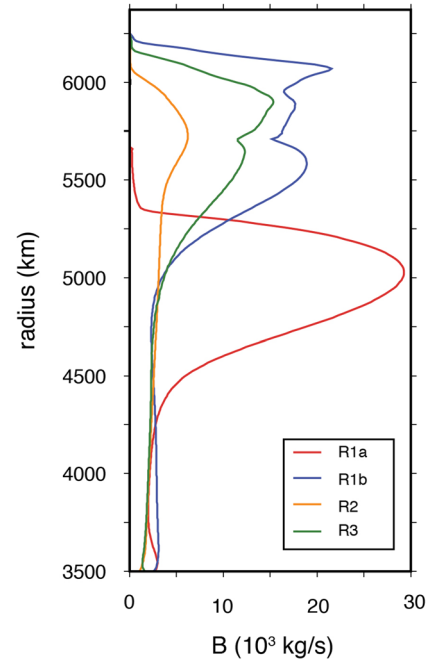


Figure 6. Plume buoyancy flux as a function of depth for plumes R1a (red), R1b (blue), R2 (orange) and R3 (green).

Fig. 6 shows the depth dependence of buoyancy flux B for each plume model. The variations of B with depth primarily reflects the position of the buoyant plume head. Buoyancy flux also increases from the lower mantle to the upper mantle if the viscosity in the upper mantle is lower. The plume in model R1b has the largest upper-mantle buoyancy flux of $B = 20 \times 10^3 \text{ kg s}^{-1}$, which is more than twice as large as B estimated for Hawaii. R1b is not in steady state as the plume head is still rising in the upper mantle. We expect a transient reduction of B for a long-lived plume supported swell (such as Hawaii) after the plume head spreads and cools beneath the lithosphere. The values of B in Table 1 apply to the plume

tail at 2500 km depth. These estimates may be most comparable to estimates of buoyancy flux beneath hotspots (Goes *et al.* 2004).

4 SEISMIC WAVE PROPAGATION THROUGH PLUME MODELS

We analyse the waveform differences between the background model and the four seismic models using two approaches. In the first approach, we measure S - and P -wave delay time by cross-correlation. In the second approach, we measure instantaneous phase differences (Bozdağ *et al.* 2011), which allow for small-amplitude diffracted arrivals to be analysed.

4.1 Traveltime delays from waveform correlation

The P and S delay times (ΔT_P and ΔT_S) (Fig. 7) are defined by waveform cross-correlation functions. We determine the delay using the first upswing and maximum, which correspond to about an 8 s long wave segment. Given the slight differences between the waveforms for the background and plume models, we modify the cross-correlation window to determine how the delay times vary as a function of window length. From the variability we estimate that our measurements of delay times have uncertainties of about ± 0.1 s at a period of 10 s. The uncertainties are slightly higher at longer periods.

For plumes R1b, R2 and R3, which have plume heads in the upper mantle, the form of ΔT_P and ΔT_S up to $X = 10^\circ$ is determined by the shape and width of the plume head in the upper mantle. The peak delay is recorded near the plume axis at about $X = 4^\circ$ when P and S propagate steeply through the centre of the plume head. Model R2 produces the largest ($\Delta T_S = 15$ s and $\Delta T_P = 4$ s) and broadest imprints of ΔT_P and ΔT_S because it has the strongest

and widest plume head beneath the lithosphere. At $X > 10^\circ$, ΔT_P and ΔT_S decrease smoothly as P and S traverse the plume tail at progressively larger depth. For plume model R3, the weakest and thinnest plume, S and P delays are approximately 0.4 and 0.1 s, respectively. The P and S delays due to plume R1a begin at about $X = 10^\circ$ behind the plume axis when P and S turn in the lower mantle. For all models, the P delay is recorded slightly earlier than the S delay because, at the same period, P has a broader Fresnel zone than S .

Fig. 8 shows ΔT_S as a function of X along the axis through the event and plume (i.e. $Y = 0$) for periods of $T > 10$ s, $T > 20$ s and $T > 40$ s, and computed using ray theory. The ray-theoretical delay times and the delay times determined from waveform correlation have the same character. The maxima in ΔT_S at $X < 10^\circ$ reflect the complexity of the seismic structure of the plume head. Ray theory predicts these maxima to be strongly peaked. The maxima in ΔT_S are smallest and smoothest when measured from the longest period waveforms because, at increasingly longer periods, the Fresnel zones widen.

At $X > 10^\circ$, when S samples the plume tail in the lower mantle (for models R1b, R2 and R3), the ray-theoretical ΔT_S and ΔT_P determined by cross-correlation decrease monotonically with X for three reasons. First, for increasing X , S crosses the plume tail along a shorter path. Second, ΔV_S decreases with depth (see Fig. 2), albeit slightly. Third, wave diffraction (i.e. wave front healing) causes wave delays to diminish. This effect is strongest at the longest periods. Therefore, ΔT_S is smallest when determined from waves with the longest periods and the widest Fresnel zones.

For model R2, a relatively strong plume, ΔT_S at $X = 35^\circ$ is 1.2, 1.0, and 0.8 s at periods of 10, 20, and 40 s, respectively. For model R3, the weakest and narrowest plume, ΔT_S at $X = 35^\circ$ is 0.5, 0.4, and 0.3 s at periods of 10, 20, and 40 s, respectively. These delays are about half the delays predicted by ray theory.

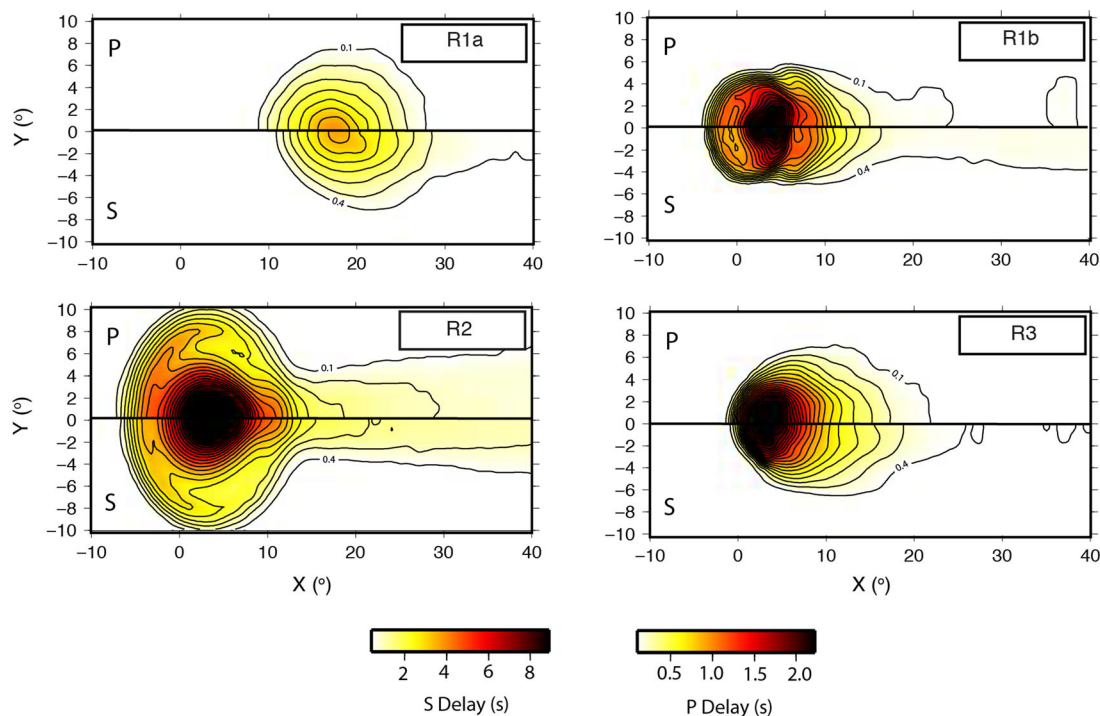


Figure 7. Cross-correlation delay times for plume models R1a, R1b, R2 and R3 as a function of X and Y . The top half and bottom half of each map show P and S delays, respectively. The S -wave delay timescale is four times wider than the P delay timescale. P -wave contours are drawn every 0.125 s, starting at 0.1 s. S -wave contours are drawn every 0.5 s, starting at 0.4 s.

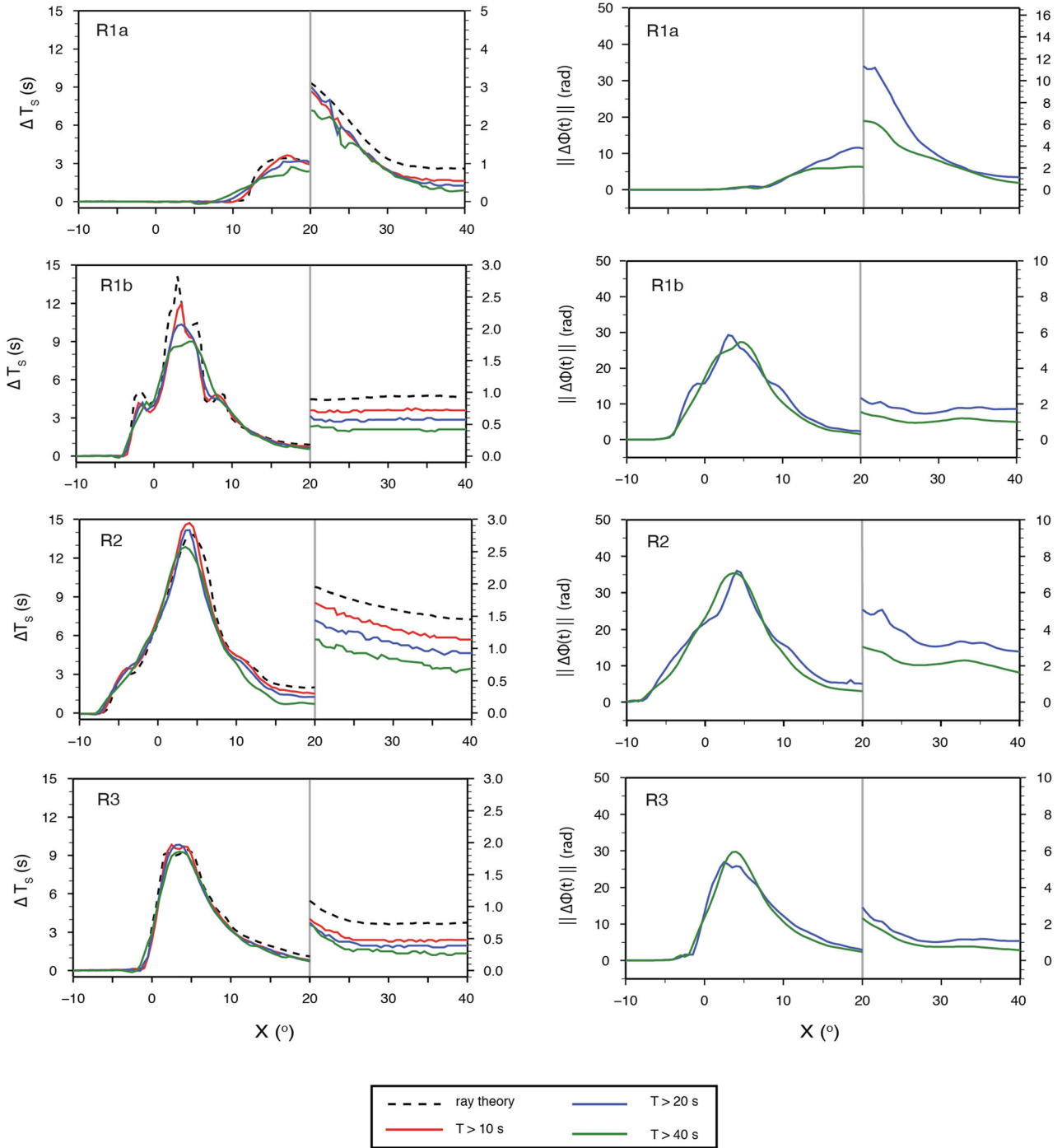


Figure 8. Left column: ΔT_s as a function of X along the earthquake-plume axis (i.e. $Y = 0$) for each of the four plume models. The dashed line shows calculated ray-theoretical delays. The solid lines show ΔT_s determined by cross-correlation of waveforms with periods larger than (red) 10, (blue) 20 and (green) 40 s. At distances greater than $X = 20$, the vertical scale is exaggerated to show detail. Right column: norm of instantaneous phase misfit measured along the earthquake-plume axis for periods larger than 20 s (blue) and periods larger than 40 s (green).

4.2 Instantaneous phase misfit

The instantaneous phase analysis (Rickers *et al.* 2012, 2013) is useful to isolate signals of wave diffraction around the plume tail. These diffractions have low amplitudes relative to direct arrivals and would contribute insignificantly to waveform cross-correlation functions. Instantaneous phase differences are independent of signal amplitude and thus not dominated by the high-amplitude direct

arrival. Instantaneous phase misfits, $\Delta\phi(t)$ are calculated for S at periods $T > 20$ s and $T > 40$ s over an extended time window of 80 s to include signal due to plume diffraction. At this relatively long period and with water-level stabilization, the analysis is not complicated by large phase mismatches. Measurements of instantaneous phase misfit are visually inspected to ensure that $\Delta\phi(t)$ is well behaved.

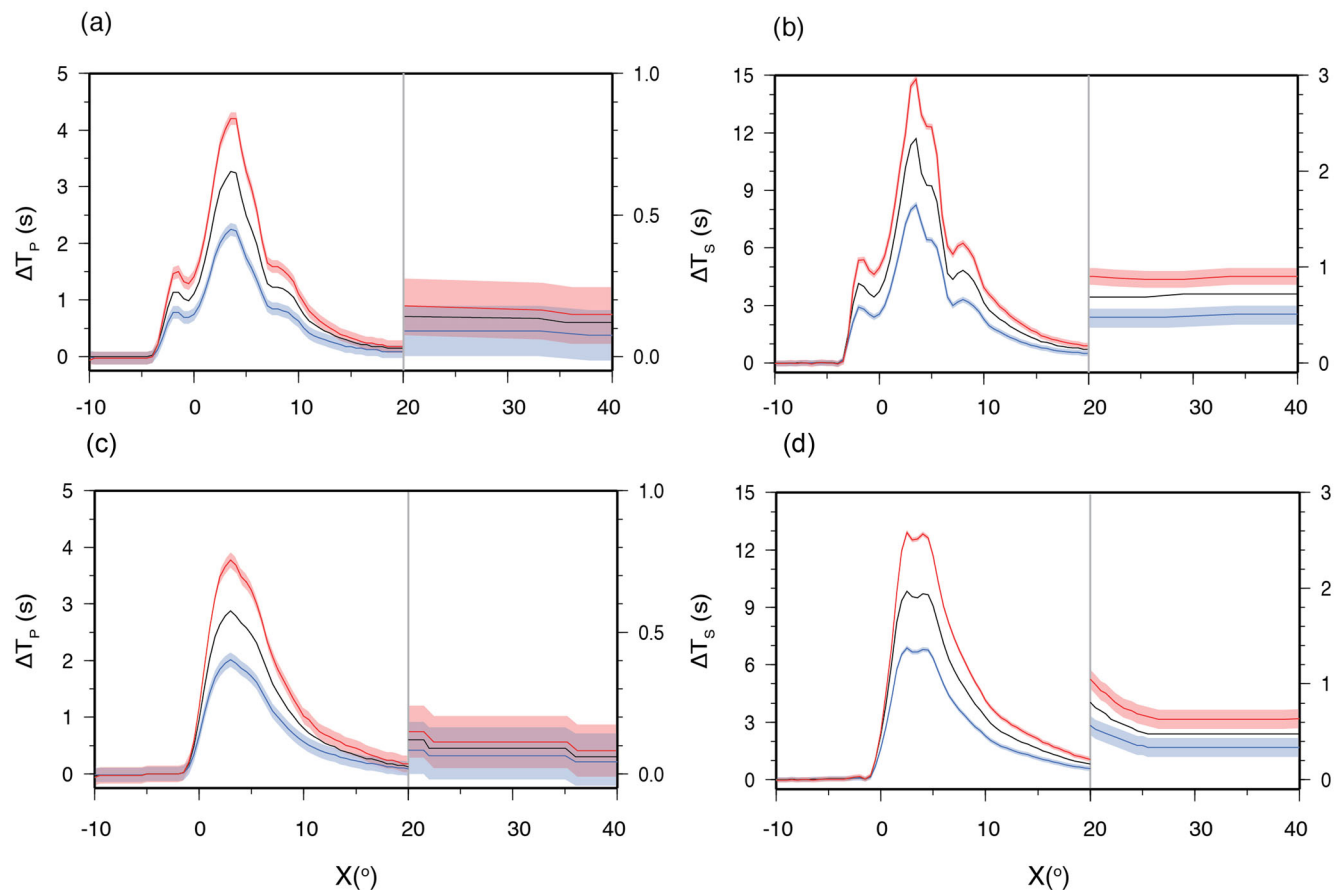


Figure 9. P (left) and S (right) delay times as a function of distance X behind the plume for models R1b (a and b) and R3 (c and d), measured at periods larger than 10 s. The shaded regions indicate the measurement uncertainty of ± 0.1 s. The black line shows delay times for models R1b and R3 (see Fig. 5). The blue and red lines show measured delay times after multiplying the P and S velocity reductions by a factor 0.7, and 1.3, respectively. These represent the upper and lower bounds of the uncertainties associated with the temperature conversion.

Fig. 8 (right column) shows the L2 norm of the instantaneous phase misfit, $||\Delta\phi(t)||$, as a function of X for the seismic models in Fig. 5. The form of $||\Delta\phi(t)||$ resembles ΔT_S determined by cross-correlation. However, $||\Delta\phi(t)||$ decays more slowly with distance because the small-amplitude diffractions contribute to the measurement of the delay. At periods of $T > 40$ s, cross-correlation measurements of R3 decay to less than 2 per cent of their maximum value at $X = 10^\circ$. Equivalently, large instantaneous phase misfits are still observed up to $X = 40^\circ$. In addition, non-zero instantaneous phase misfit values are recorded over a wider range in azimuth. These results demonstrate that, at low frequencies, the instantaneous phase measurement is more useful than time-domain waveform cross-correlation to resolve the narrow plume conduits in the lower mantle, in agreement with Rickers *et al.* (2012).

5 DISCUSSION AND CONCLUSIONS

Models R1b and R3 (see Fig. 5) are our end-member estimates of V_P and V_S reductions within the conduits in the lower mantle. The seismic structure of R1b includes up to 2 and 4 per cent reductions in V_P and V_S which delay teleseismic P and S waves by about 0.15 and 0.7 s. V_P and V_S in the tail of R3 are reduced by as much as 1.8 and 3.5 per cent and lead to P and S delays of about 0.1 and 0.45 s. The delay times depend on the chosen frequency band in which P and S are analysed because Fresnel zones broaden with decreasing

frequency. S delays for model R1b (at a distance $X = 35^\circ$ in Fig. 8) are 0.7 s for $T > 10$ s and 0.4 s for $T > 40$ s. S delays for model R3 are 0.5 s for $T > 10$ s and 0.3 s for $T > 40$ s. These delays are up to 50 per cent smaller than ray-theoretically predicted delays. To ensure that the presence of a plume head in the upper mantle is not biasing our results, in addition to the work shown, we separately modeled the upper- and lower-mantle expression of plume R1b (i.e. both just the head and just the tail). We find that delays induced by the plume head disappear entirely for distances larger than $X = 10^\circ$, and that any delay signal beyond this distance can be attributed entirely to the plume tail.

Given that plumes may have a distinct composition (Lin & van Keken 2005; Ballmer *et al.* 2013; Dannberg & Sobolev 2015) and that the conversion between temperature, composition and wave speed structure is uncertain (Cobden *et al.* 2008; Styles *et al.* 2011), we estimate that the P - and S -wave reductions are uncertain by 30 per cent. Waveform simulations indicate that the P and S delays depend linearly on the V_P and V_S reductions in agreement with previous modeling (Mercerat & Nolet 2013). If V_P and V_S are enhanced or reduced by 30 per cent, the delay times increase or decrease by 30 per cent (Fig. 9).

These delays are somewhat larger than the delays we have previously determined using 2-D modeling (Hwang *et al.* 2011). Nevertheless, we remain skeptical that faint delays in P (< 0.3 s) associated with thin thermal plumes are detectable in currently available seismic data sets. The 0.4–0.8 s delay of S waves by lower-mantle

plume conduits and the diagnostic frequency dependence should be observable when the influence of the heterogeneous crust and uppermost mantle is small. For example, recordings of abundant earthquakes in the Tonga–Fiji and Kermadec regions by a wide-aperture network of ocean-bottom seismometers (OBS) in the northeast Pacific (as sketched in Fig. 3b) would provide wave sampling of the lower mantle beneath Hawaii. Since the structure of the crust and lithosphere beneath the northeast Pacific is relatively simple, traveltimes delays accrued in the lithosphere may be estimated using plate cooling models and from delay time measurements over a broad range of source azimuths. The traveltime dispersion due to reverberations in the crust (Hwang *et al.* 2011) is different than the dispersion due to plumes and can be estimated from layered models of the oceanic crust. Ideally, such OBS network cover the ocean floor beyond the Hawaiian swell to ensure lower-mantle sampling beneath Hawaii and to record the smooth and systematic decay of the traveltime delays.

ACKNOWLEDGEMENTS

Numerical wavefield simulations were performed both at the Swiss National Supercomputing Centre as part of the CHRONOS project ch1 and at the Stampede supercomputer through XSEDE allocation TG-EAR150001. This research is supported by NSF Grant EAR-0855487. Support from the Scott Turner Research Grant facilitated travel for RM to ETH Zürich.

REFERENCES

- Albers, M. & Christensen, U.R., 1996. The excess temperature of plumes rising from the core–mantle boundary, *Geophys. Res. Lett.*, **23**(24), 3567–3570.
- Allen, R.M., 2002. Imaging the mantle beneath Iceland using integrated seismological techniques, *J. geophys. Res.*, **107**(B12), 1–16.
- Ballmer, M., van Keken, P. & Ito, G., 2015. Hotspots, large igneous provinces, and melting anomalies, in *Treatise on Geophysics*, 2nd edn, pp. 393–459, ed. Schubert, G. Elsevier, Oxford.
- Ballmer, M.D., Ito, G., Wolfe, C.J. & Solomon, S.C., 2013. Double layering of a thermochemical plume in the upper mantle beneath Hawaii, *Earth planet. Sci. Lett.*, **376**, 155–164.
- Bijwaard, H. & Spakman, W., 1999. Tomographic evidence for a narrow whole mantle plume below Iceland, *Earth planet. Sci. Lett.*, **166**(3–4), 121–126.
- Boschi, L., Becker, T.W. & Steinberger, B., 2007. Mantle plumes: dynamic models and seismic images, *Geochem. Geophys. Geosyst.*, **8**(10), 1–20.
- Boschi, L., Becker, T.W. & Steinberger, B., 2008. On the statistical significance of correlations between synthetic mantle plumes and tomographic models, *Phys. Earth planet. Inter.*, **8**(10), 230–238.
- Bossmann, A.B. & van Keken, P.E., 2013. Dynamics of plumes in a compressible mantle with phase changes: implications for phase boundary topography, *Phys. Earth planet. Inter.*, **224**, 21–31.
- Bozdağ, E., Trampert, J. & Tromp, J., 2011. Misfit functions for full waveform inversion based on instantaneous phase and envelope measurements, *Geophys. J. Int.*, **185**(2), 845–870.
- Cobden, L., Goes, S., Cammarano, F. & Connolly, J.A.D., 2008. Thermochemical interpretation of one-dimensional seismic reference models for the upper mantle: evidence for bias due to heterogeneity, *Geophys. J. Int.*, **175**(2), 627–648.
- Connolly, J.A.D., 2005. Computation of phase equilibria by linear programming: a tool for geodynamic modeling and its application to subduction zone decarbonation, *Earth planet. Sci. Lett.*, **236**(1–2), 524–541.
- Courtier, A.M. *et al.*, 2007. Correlation of seismic and petrologic thermometers suggests deep thermal anomalies beneath hotspots, *Earth planet. Sci. Lett.*, **264**, 308–316.
- Dannberg, J. & Sobolev, S.V., 2015. Low-buoyancy thermochemical plumes resolve controversy of classical mantle plume concept, *Nature Commun.*, **6**, doi:10.1038/ncomms7960.
- Diego Mercierat, E. & Nolet, G., 2013. On the linearity of cross-correlation delay times in finite-frequency tomography, *Geophys. J. Int.*, **192**(2), 681–687.
- Farnetani, C.G., 1997. Excess temperature of mantle plumes: the role of chemical stratification across D, *Geophys. Res. Lett.*, **24**(13), 1583–1586.
- French, S.W. & Romanowicz, B., 2015. Broad plumes rooted at the base of the earth's mantle beneath major hotspots, *Nature*, **525**(7567), 95–99.
- Goes, S., Cammarano, F. & Hansen, U., 2004. Synthetic seismic signature of thermal mantle plumes, *Earth planet. Sci. Lett.*, **218**(3–4), 403–419.
- Gokhberg, A. & Fichtner, A., 2015. Full-waveform inversion on heterogeneous HPC systems, *Comput. Geosci.*, doi:10.1016/j.cageo.2015.12.013.
- Herzberg, C., Ratterron, P. & Zhang, J., 2000. New experimental observations on the anhydrous solidus for peridotite KLB-1, *Geochem. Geophys. Geosyst.*, **1**(11), doi:10.1029/2000GC000089.
- Hwang, Y.K., Ritsema, J., van Keken, P.E., Goes, S. & Styles, E., 2011. Wavefront healing renders deep plumes seismically invisible, *Geophys. J. Int.*, **187**(1), 273–277.
- Jarvis, G.T. & McKenzie, D.P., 1980. Convection in a compressible fluid with infinite prandtl number, *J. Fluid Mech.*, **96**(03), 515–583.
- Karato, S.I. & Wu, P., 1993. Rheology of the upper mantle—a synthesis, *Science*, **260**(5109), 771–778.
- King, S.D. & Ritsema, J., 2000. African hot spot volcanism: small-scale convection in the upper mantle beneath cratons, *Science*, **19**(1), 181–188.
- Kumagai, I., Davaille, A., Kurita, K. & Stutzmann, E., 2008. Mantle plumes: thin, fat, successful, or failing? Constraints to explain hot spot volcanism through time and space, *Geophys. Res. Lett.*, **35**(16), 1–5.
- Lay, T., Hernlund, J. & Buffett, B.A., 2008. Core-mantle boundary heat flow, *Nature Geosci.*, **1**(1), 25–32.
- Lin, S.C. & van Keken, P.E., 2005. Multiple volcanic episodes of flood basalts caused by thermochemical mantle plumes, *Nature*, **436**(7048), 250–252.
- Lin, S.C. & van Keken, P.E., 2006. Dynamics of thermochemical plumes: 2. Complexity of plume structures and its implications for mapping mantle plumes, *Geochem. Geophys. Geosyst.*, **7**(3), doi:10.1029/2005GC001072.
- Malcolm, A.E. & Trampert, J., 2011. Tomographic errors from wave front healing: more than just a fast bias, *Geophys. J. Int.*, **185**(1), 385–402.
- Montelli, R., Nolet, G., Dahlen, F.A., Masters, G., Engdahl, E.R. & Hung, S.-H., 2004. Finite-frequency tomography reveals a variety of plumes in the mantle, *Science*, **303**(5656), 338–343.
- Morgan, W.J., 1971. Convection plumes in the lower mantle, *Nature*, **230**, 42–43.
- Nolet, G. & Dahlen, F.A., 2000. Wave front healing and the evolution of seismic delay times, *J. geophys. Res.*, **105**(19), 19 043–19 054.
- Rickers, F., Fichtner, A. & Trampert, J., 2012. Imaging mantle plumes with instantaneous phase measurements of diffracted waves, *Geophys. J. Int.*, **190**(1), 650–664.
- Rickers, F., Fichtner, A. & Trampert, J., 2013. The Iceland–Jan Mayen plume system and its impact on mantle dynamics in the North Atlantic region: evidence from full-waveform inversion, *Geophys. J. Int.*, **367**(1), 39–51.
- Samuel, H. & Bercovici, D., 2006. Oscillating and stagnating plumes in the Earth's lower mantle, *Earth planet. Sci. Lett.*, **248**(1–2), 75–90.
- Samuel, H. & Farnetani, C.G., 2003. Thermochemical convection and helium concentrations in mantle plumes, *Earth planet. Sci. Lett.*, **207**(1–4), 39–56.
- Schmandt, B., Dueker, K., Humphreys, E. & Hansen, S., 2012. Hot mantle upwelling across the 660 beneath Yellowstone, *Earth planet. Sci. Lett.*, **331–332**, 224–236.
- Shen, Y., Solomon, S.C., Bjarnason, I. & Wolfe, C.J., 1998. Seismic evidence for a lower mantle origin of the Iceland mantle plume, *Nature*, **395**, 62–65.
- Sleep, N.H., 1990. Hotspots and mantle plumes: some phenomenology, *Geology*, **95**, 6715–6736.

- Stixrude, L. & Lithgow-Bertelloni, C., 2011. Thermodynamics of mantle minerals—II. Phase equilibria, *Geophys. J. Int.*, **184**(3), 1180–1213.
- Styles, E., Goes, S., van Keken, P.E., Ritsema, J. & Smith, H., 2011. Synthetic images of dynamically predicted plumes and comparison with a global tomographic model, *Earth planet. Sci. Lett.*, **311**(3–4), 351–363.
- Wilson, J.T., 1963. A possible origin of the hawaiian islands, *Can. J. Phys.*, **41**(6), 863–870.
- Wolfe, C.J., Solomon, S.C., Laske, G., Collins, J.A., Detrick, R.S., Orcutt, J.A., Bercovici, D. & Hauri, E.H., 2009. Mantle shear-wave velocity structure beneath the Hawaiian hot spot, *Science*, **326**(5958), 1388–1390.
- Workman, R.K. & Hart, S.R., 2005. Major and trace element composition of the depleted MORB mantle (DMM), *Earth planet. Sci. Lett.*, **231**(1–2), 53–72.
- Zerr, A., Diegeler, A. & Boehler, R., 1998. Solidus of Earth’s deep mantle, *Science*, **281** 243–246.